CASL-U-2017-1390-000

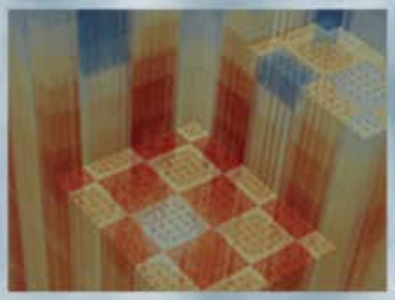

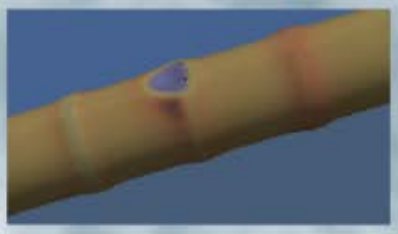

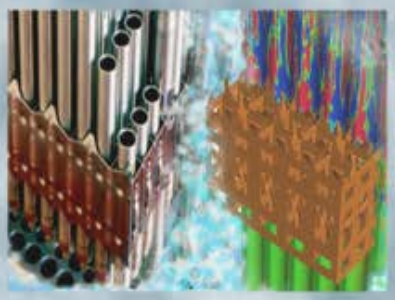

Reference Computational Meshing Strategy for Computational Fluid Dynamics Simulation of Departure from Nucleate Boiling

W. David Pointer,
Oak Ridge National Laboratory

July 14, 2017

U.S. DEPARTMENT OF ENERGY | Nuclear Energy

1.1.REVISION LOG

Revision	Date	Affected Pages	Revision Description
0	7-14-17	All	Initial Release

Document pages that are:

Unlimited _____All_____

Export Controlled _____None_____

IP/Proprietary/NDA Controlled_____None_____

Sensitive Controlled_____None_____

Requested Distribution:

To: CASL SLT

Emilio Baglietto, CASL THM Lead

Copy: Chris Jones, CASL VVI Lead

Yixing Sung,CASL DNB Challenge Problem Lead

Approved for Public Release

EXECUTIVE SUMMARY

The objective of this effort is to establish a strategy and process for generation of suitable computational mesh for computational fluid dynamics simulations of departure from nucleate boiling in a 5 by 5 fuel rod assembly held in place by PWR mixing vane spacer grids. This mesh generation process will support ongoing efforts to develop, demonstrate and validate advanced multi-phase computational fluid dynamics methods that enable more robust identification of dryout conditions and DNB occurrence.

Building upon prior efforts and experience, multiple computational meshes were developed using the native mesh generation capabilities of the commercial CFD code STAR-CCM+. These meshes were used to simulate two test cases from the Westinghouse 5 by 5 rod bundle facility. The sensitivity of predicted quantities of interest to the mesh resolution was then established using two evaluation methods, the Grid Convergence Index method and the Least Squares method.

This evaluation suggests that the Least Squares method can reliably establish the uncertainty associated with local parameters such as vector velocity components at a point in the domain or surface averaged quantities such as outlet velocity magnitude. However, neither method is suitable for characterization of uncertainty in global extrema such as peak fuel surface temperature, primarily because such parameters are not necessarily associated with a fixed point in space. This shortcoming is significant because the current generation algorithm for identification of DNB event conditions relies on identification of such global extrema. Ongoing efforts to identify DNB based on local surface conditions will address this challenge.

CONTENTS

FIGURES

TABLES

ACRONYMS

CASL Consortium for Advanced Simulation of Light Water Reactors
CHF Critical Heat Flux
CFD computational fluid dynamics
DNB departure from nucleate boiling
GCI grid convergence index
LSQ least squares
PWR pressurized water reactor

1. OBJECTIVE

Nucleate boiling is an efficient cooling strategy in which the energy produced by a heat source results in the formation of small bubbles on the heater surface. These bubbles grow until they become large enough to detach from the surface and liquid coolant then rushes in to quench the surface and begin the process anew. Departure from nucleate boiling, or DNB, describes a condition in which the thermal energy produced by a heat source that is being cooled by nucleate boiling of the coolant in which it is immersed becomes sufficiently large to support the formation of substantial dry regions on the heater surface. When this occurs, liquid coolant can no longer reach the surface in that region, boiling can no longer occur on the surface, and the region of vapor on the dry wall is unable to remove as much heat as the boiling coolant it replaces. This localized loss of cooling results in a rapid localized rise in the temperature of the heat source can result in significant structural damage.

The Consortium for Advanced Simulation of Light Water Reactors is developing a high-resolution capability for the prediction of flow conditions in which DNB is likely to occur in a nuclear fuel assembly based on multi-phase computational fluid dynamics, or CFD, methods. The objective of this work is to develop a baseline procedure for the development of CFD meshes which describe and discretize the application geometry in the assessment of DNB.

2. APPLICATION

The focus of the CASL effort to enable predictive DNB simulations is the development of improved thermal hydraulic closure models within the framework of a general finite volume multi-phase CFD method. [1] The principal validation benchmark data set for qualification of this capability is derived from experiments completed by Westinghouse in a 5 x 5 pressurized water reactor (PWR) fuel rod bundle experiment at Columbia University's Heat Transfer Research Facility. [2]

2.1. Geometry

The 5 x 5 rod bundle array uses 25 electrically heated rods of uniform diameter that are arranged in a regular square lattice inside a square pressure boundary as shown in Figure 1. The rod array is held in place by 5 spacer grids of the split mixing vane type that are evenly spaced as shown in the illustration. While the heated region is shorter than a typical PWR fuel assembly, prototypic grid span lengths were maintained. The heated tests employ a non-uniform radial power profile within the bundle, with 6 hot pins having slightly elevated power levels. The axial power distribution is uniform. An array of thermocouples captures individual subchannel coolant temperatures near the outlet of the heated region. Additional thermocouples within the heated rods provide capability to detect critical heat flux (CHF) or DNB.

Detailed bundle and spacer grid dimensions are imported directly to the computational model from a three-dimensional CAD description of the facility.

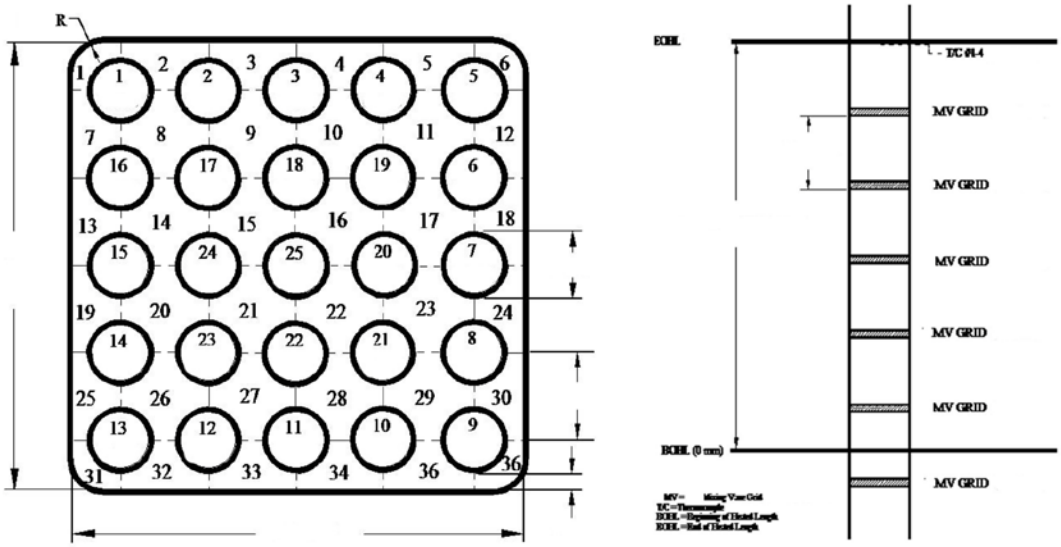

(a) (b)

Figure 1. Lateral and axial geometric configuration of the 5 x 5 rod bundle geometry considered.

2.2. Flow Conditions Considered

Two flow conditions were selected from the extensive test matrix to support development of the computational model, as shown in Table 1. The first case, based on run 4, is an isothermal single-phase test. The second case, based on run 9, is a heated case with substantial inlet subcooling and minimal vapor production.

Table 1. Operating conditions to be modeled,

Run	Outlet Pressure (bar)	Inlet Temperature (°C)	Mass Flux (kg/m^2s)	Average Pin Heat Flux (W/m2)
4	69.962	53.225	3989.320	0.000
9	159.939	310.833	3647.168	61.183

3. GEOMETRIC SIMPLIFICATIONS

The spacer grid, by design has many contact points with the electrically heated fuel rods. In the CFD models developed from this geometry, these contacts are eliminated by expanding the radius of the fuel pin by the thickness of the spacer grid structure and trimming away the spacer components nearest the pin surface, as shown in Figure 2. This geometric simplification eliminates the need to concentrate very small cells near the contact points in order to resolve the narrow spaces. Perhaps more importantly, it eliminates the need to mesh the thin elements of the spacer itself and simulate the conductive heat transfer through the spacer components.

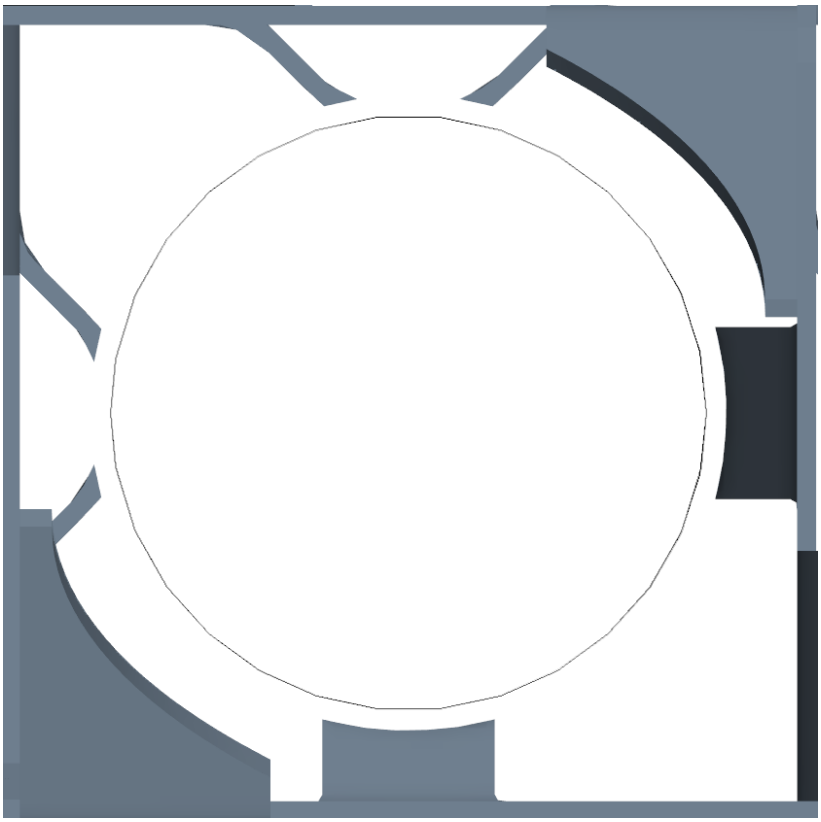

Figure 2. Illustration of simplified spacer grid with rod contacts removed.

4. MESH GENERATION

All computational meshes shown were generated using the native mesh generation capabilities of the commercial CFD code STAR-CCM+. [3] Generated meshes use the trimmed mesh method in which a uniform hexahedral mesh is generated in a volume larger than the region of interest, refined locally based on curvature and user-defined surface specifications, and then trimmed away in regions falling outside the domain of interest. This results in many polyhedral cells near surfaces, which can be detrimental to solution stability, so a regular prismatic extrusion layer is created near the surface.

Following the method successfully applied by Brewster, et al. [4], the cell size specifications for the automatic mesh generation procedure is derived from a single parameter labeled the base cell size. For this problem, cells in the bulk coolant region have a dimension equivalent to the base cell size

and cells that contact the spacer grid are refined to one-half of the base cell size. A uniform prismatic surface extrusion layer with a thickness of 0.15 mm was found to assure applicability of the preferred turbulence model and was applied to all surfaces. Surface refinement parameters are set so that two cells adjacent to any surface are refined. Code default values for curvature and gap parameters were utilized. Unlike reference [4], the model is constructed as a single continuous region with no liquid-liquid interfaces. Solid structures of the rods were not meshed in the present models, but can be easily appended by extrusion as a consequence of the geometric simplification discussed in the previous section.

The mesh distribution across the lateral cross-section of the 5 x 5 rod bundle model is shown for a base cell size of 0.3 mm in Figures 3 - 5, where the cross-sections are just below the grid, at the center of the grid and just below the tips of the mixing vanes, respectively. The impact of the base cell size can be seen in Figure 6, where the base cell size parameter is varied from 0.3 mm to 1.0 mm. The number of computational elements used in each mesh is shown in Table 2.

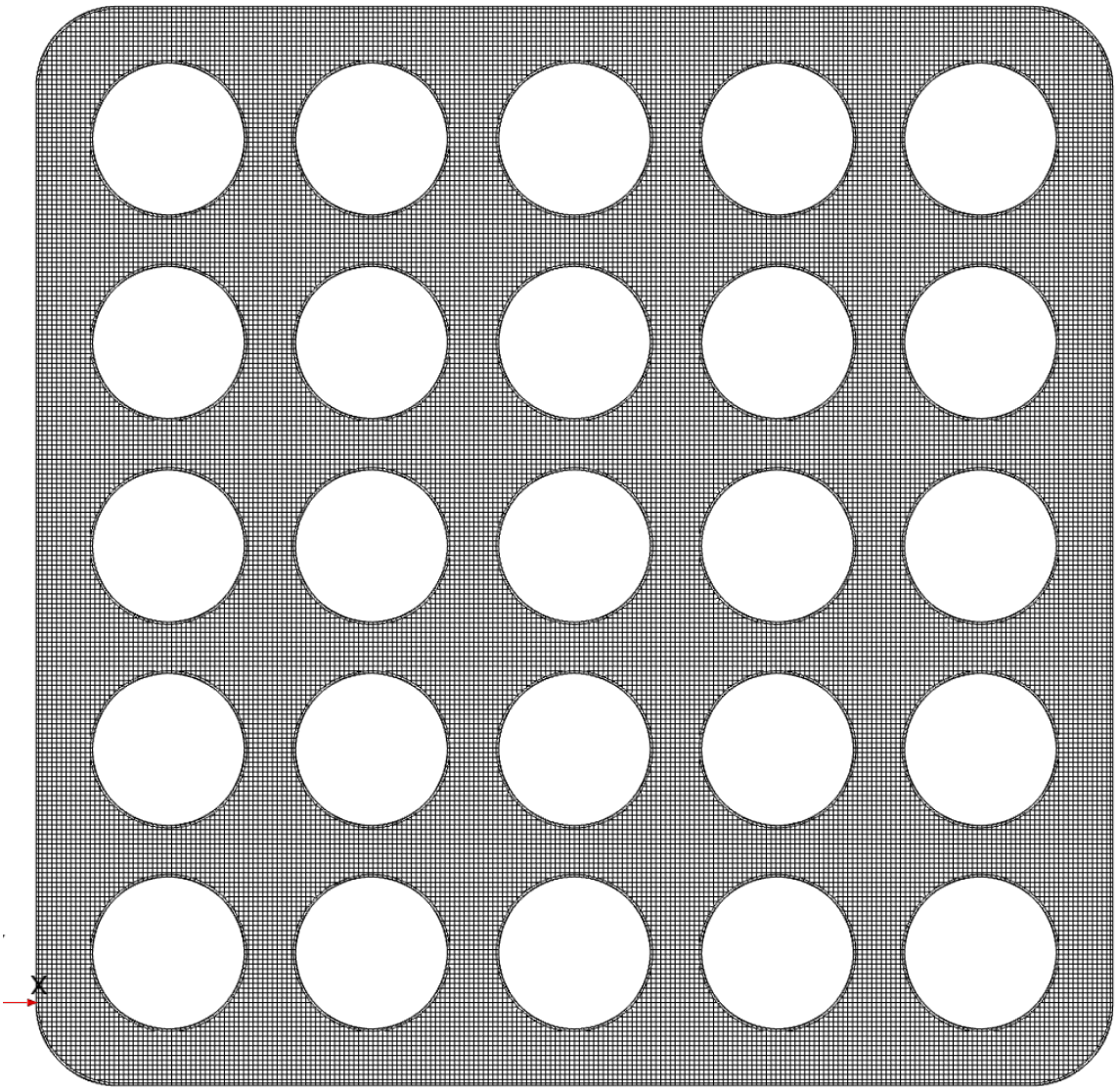

Figure 3. Mesh distribution in lateral cross-section just below the spacer grid with a base cell size of 0.3 mm.

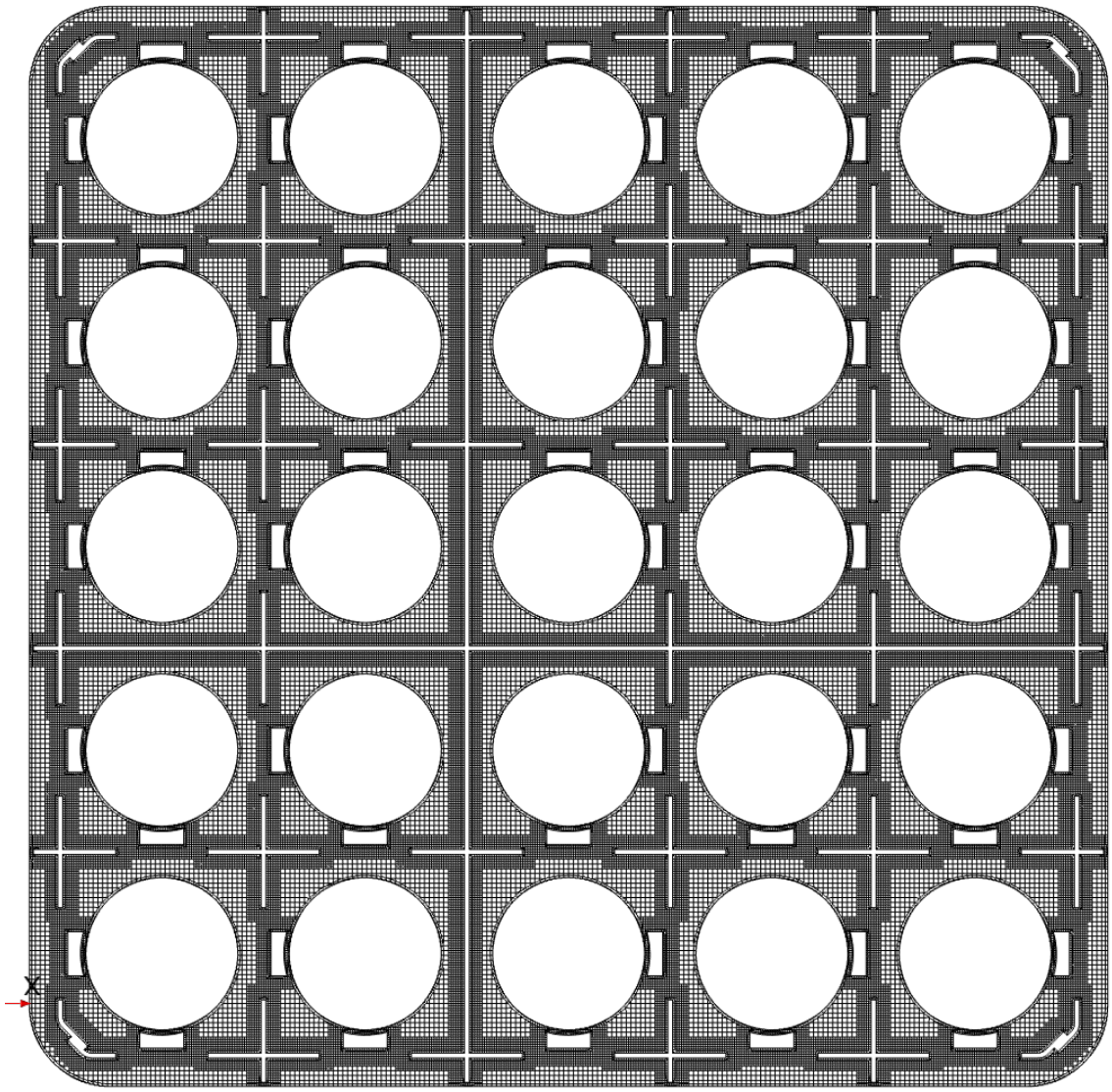

Figure 4. Mesh distribution in lateral cross-section at the center of the spacer grid with a base cell size of 0.3 mm.

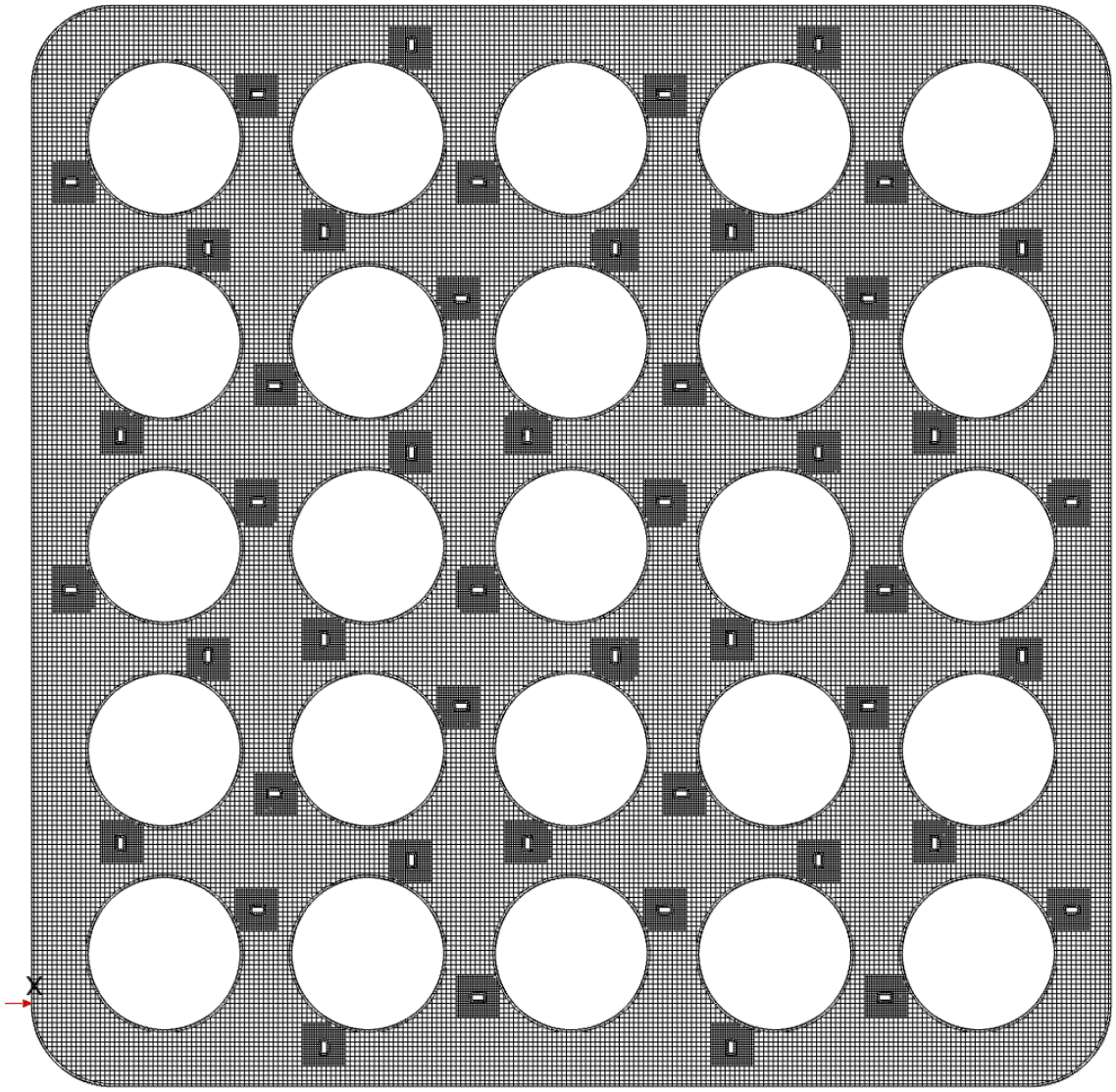

Figure 5. Mesh distribution in lateral cross-section just below the tip of the spacer grid mixing vane with a base cell size of 0.3 mm.

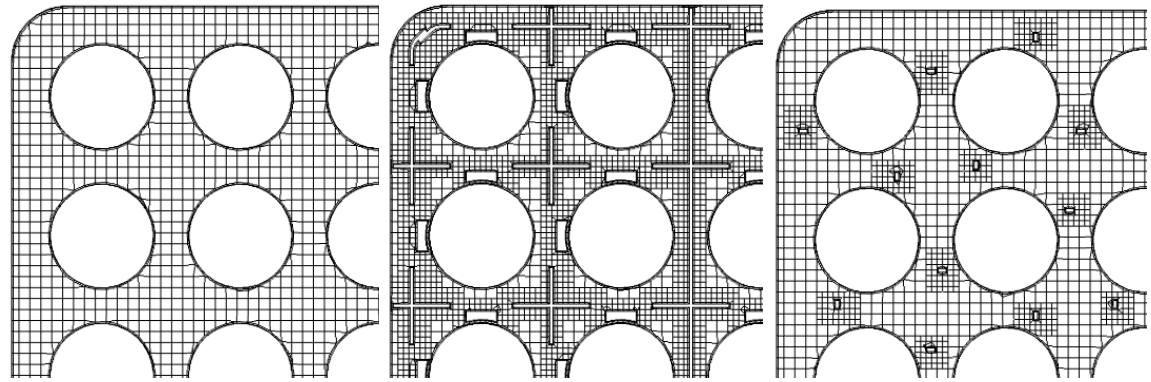

Base Size = 1.0 mm

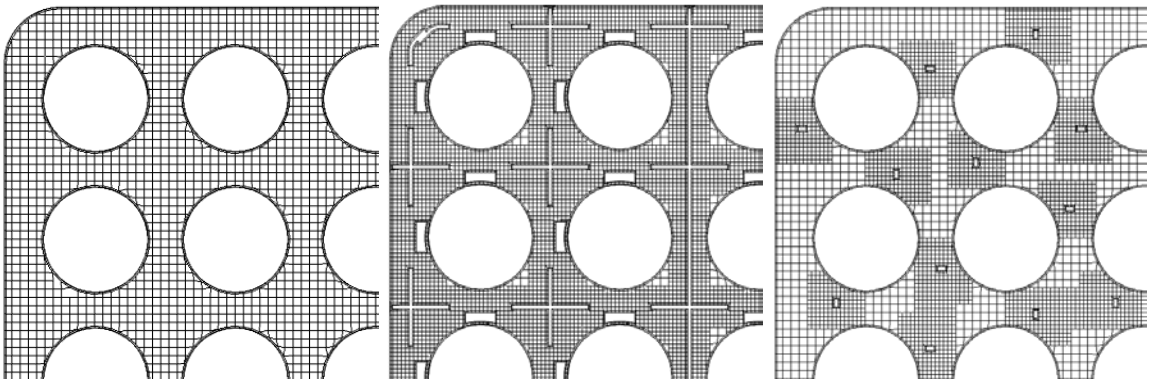

Base Size = 0.75 mm

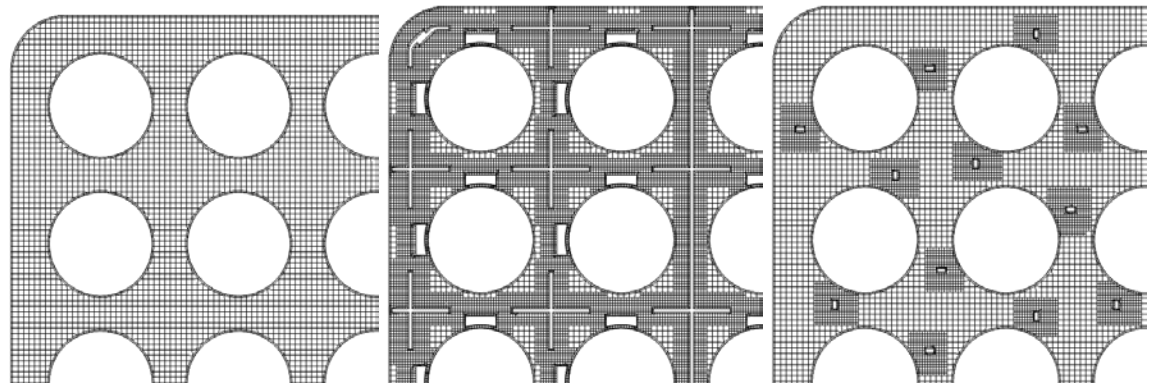

Base Size = 0.5 mm

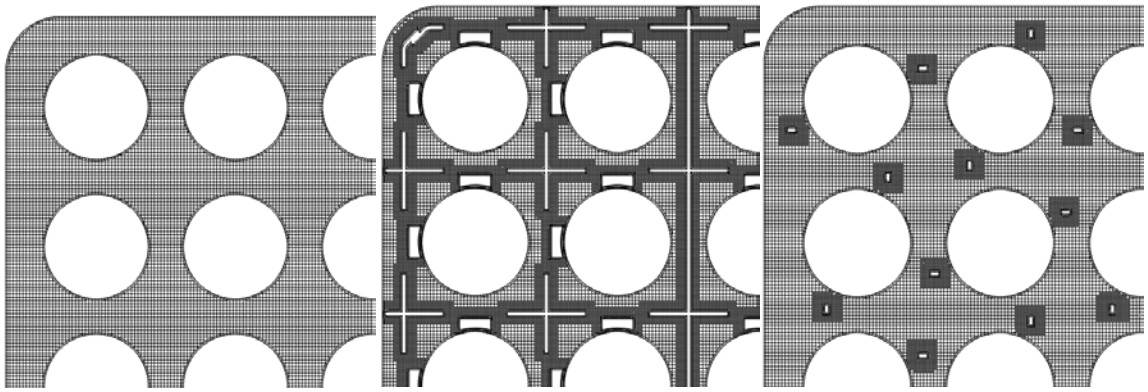

Base Size = 0.3 mm

Figure 6. Variation in mesh distribution with changes in base cell size parameter.

Table 2. Number of elements used in each model, as a function of base cell size parameter.

Base Cell Size (m)	# of Elements
1.00E-03	17,182,514
7.50E-04	39,653,550
5.00E-04	109,797,000
3.00E-04	421,845,500

5. MODEL DESCRIPTION

STAR-CCM+ is a general-purpose analysis package for thermal and compressible/incompressible fluid flow phenomena based on the finite volume formulation. It supports using generic polyhedral mesh elements and provides several approaches for fully parallel generation of conformal computational meshes describing complex geometries. Solutions are obtained via the SIMPLE algorithm with Rhie-Chow interpolation for velocity to pressure coupling and are accelerated with algebraic multi-grid preconditioning. Energy-to-flow coupling is treated using a split operator methodology. The code provides second-order accuracy in its resolution of spatial and temporal phenomena, but all calculations in the present study are steady state.

The Eulerian-Eulerian dispersed phase models implemented in STAR-CCM+ are the foundation for CASL's development of an advanced boiling simulation capability. More details of CASL's efforts with the Eulerian-Eulerian CASL closure model can be found in Reference 1. The Eulerian-Eulerian dispersed phase model is implemented as an n-fluid n-field model with the following conservation equations:

$$\frac{\partial}{\partial t}(\alpha_k \rho_k) + \boldsymbol{\nabla} \cdot (\alpha_k \rho_k \boldsymbol{u}_k) = (\dot{m}_{ki} - \dot{m}_{ik}), \tag{1}$$

$$\frac{\partial}{\partial t}(\alpha_k \rho_k \boldsymbol{u}_k) + \boldsymbol{\nabla} \cdot (\alpha_k \rho_k \boldsymbol{u}_k \boldsymbol{u}_k) - \boldsymbol{\nabla} \cdot \left(\alpha_k (\boldsymbol{\tau}_k - \boldsymbol{\tau}_k')\right) = \alpha_k \nabla p + \alpha_k \rho_k \boldsymbol{g} + \boldsymbol{M}, \text{ and} \tag{2}$$

$$\frac{\partial}{\partial t}(\alpha_k \rho_k e_k) + \boldsymbol{\nabla} \cdot (\alpha_k \rho_k \boldsymbol{u}_k e_k) - \boldsymbol{\nabla} \cdot (\alpha_k \lambda_k \nabla T_k) = Q, \text{ where} \tag{3}$$

$$\boldsymbol{M} = \boldsymbol{F}_{Drag} + \boldsymbol{F}_{Lift} + \boldsymbol{F}_{Turb.Disp.} + \boldsymbol{F}_{Wall\,Lub.} + \boldsymbol{F}_{Virt.Mass} + \dot{m}_{ki}\boldsymbol{u}_i - \dot{m}_{ik}\boldsymbol{u}_k. \tag{4}$$

The conservation equations are written for phase *k* such that α_k is the volume fraction of phase *k*, and $\dot{m}_{ki}$ is the mass transfer rate from phase *k* to phase *i*.

The present model uses a simplified closure model set, described as the generation 1A model. The default wall heat partitioning, bubble nucleation and bubble departure models are applied. The bubble drag force model of Tomiyama is applied with a constant lift force coefficient model where the coefficient is set to zero. Turbulence is modeled using the standard k-epsilon model with the high y+ wall treatment.

The convergence criterion for STAR-CCM+ was defined as reduction of all conservation equation residuals by 4 orders of magnitude, or reducing the normalized residuals below 10^{-4}. However, residual normalization can be deceptive in two-phase simulations because the simulations are typically initialized with single-phase flow conditions. Therefore, asymptotic convergence of flow conditions are also monitored at selected positions within the model.

6. GRID CONVERGENCE ASSESSMENT

6.1. Grid Convergence Index Procedure

The American Society of Mechanical Engineers Standard for Verification and Validation in Computational Fluid Dynamics and Heat Transfer, known as ASME V&V 20, was established in 2009 to define requirements for quality assurance of CFD results submitted to ASME journals. As part of the standard, a five-step procedure is defined for evaluation of the uncertainty in CFD code predictions arising from the mesh discretization employed.

In the Grid Convergence Index (GCI) method, a set of computational meshes are developed to describe the problem of interest and the characteristic length scale of the mesh elements is calculated by

$$h = \left[\left(\sum_{i=1}^{N} \Delta V_i\right)/N\right]^{1/3} \tag{5}$$

where V_i is the volume of a given element i. Then simulations are completed to the same convergence criteria using at least three meshes with different characteristic element dimensions. The desired quantity of interest, f_i, is extracted from each of the simulation with a characteristic mesh size h_i. For $h_1 > h_2 > h_3$, the apparent order of convergence, p, is iteratively evaluated from the expression

$$p = \left[1/\ln(r_{21})\right]\left[\ln\left|\varepsilon_{32}/\varepsilon_{21}\right| + q(p)\right] \tag{6}$$

$$q(p) = \ln\left(\frac{r_{21}^{p} - s}{r_{32}^{p} - s}\right) \tag{7}$$

$$s = 1 \cdot \mathrm{sign}(\varepsilon_{32}/\varepsilon_{21}) \tag{8}$$

where $r_{21} = h_1/h_2$, $r_{32} = h_2/h_3$, $\varepsilon_{32} = f_3 - f_2$, and $\varepsilon_{21} = f_2 - f_1$.

Using these calculated values, a Richardson extrapolation is performed to find the extrapolated mesh converged value of the quantity of interest, f.

$$f_{ext}^{21} \_ (r_{21}{}^{p} f_1 - f_2) \tag{9}$$

$$f_{ext}^{32} \_ (r_{32}{}^{p} f_2 - f_3) \tag{10}$$

The grid convergence error is then estimated by

$$\varepsilon_{GCI}^{21} = |f_1 - f_2| \tag{11}$$

and

$$\varepsilon_{ext}^{21} = |f_{ext}^{21} - f_2| \tag{12}$$

From these error estimates, the uncertainty U_{GCI}, expressed as f_1 +/- U_{GCI}, is then given by

$$U_{GCI} = \frac{F_s \cdot \varepsilon_{GCI}^{21}}{r_{21}^{p} - 1} \tag{13}$$

or by

$$U_{ext} = \frac{F_s \cdot \varepsilon_{ext}^{21}}{r_{21}^{p} - 1} \tag{14}$$

where Fs is the so-called Safety Factor, which has a value of 3 for unstructured mesh applications.

This method can only be applied in situations in which successive refinements result in convergence to an extrapolated value. If we define $R = \varepsilon_{21}/\varepsilon_{32}$, then R must be positive and less than one for this method to be successfully applied. Unstructured mesh CFD simulations rarely exhibit this property and are more often oscillatory convergent. For this reason, the Least Squares Method is also applied.

6.2. Least Squares Method Procedure

The Least Squares Method (LSQ) of Eca and Hoekstra [5] provides an alternative procedure that is more broadly applicable to oscillatory grid convergence or even divergence. The convenient form expressed in [6] is used in these studies. If Richardson extrapolation is defined as

$$\bar{f} = f_k - \alpha h_k^{\tilde{p}} \tag{15}$$

then an error function can be formed and minimized to find

$$\alpha = \frac{n_g \sum_1^{n_g} f_k\, h_k^{\tilde{p}} - \left(\sum_1^{n_g} f_k\right)\left(\sum_1^{n_g} h_k^{\tilde{p}}\right)}{n_g \sum_1^{n_g} h_k^{2\tilde{p}} - \left(\sum_1^{n_g} h_k^{\tilde{p}}\right)^2} \tag{16}$$

$$\bar{f} = \frac{\sum_1^{n_g} f_k - \alpha \sum_1^{n_g} h_k^{\tilde{p}}}{n_g} \tag{17}$$

$$\sum_1^{n_g} f_k\, h_k^{\tilde{p}} \ln h_k - \bar{f} \sum_1^{n_g} h_k^{\tilde{p}} \ln h_k - \alpha \sum_1^{n_g} h_k^{2\tilde{p}} \ln h_k = 0 \tag{18}$$

which is solved for $\tilde{p}$. Then uncertainties are estimated by

$$\begin{array}{c} 0.95 \le \tilde{p} \le 2.05 \\ 0 < \tilde{p} \le 0.95 \\ \tilde{p} \ge 2.05 \\ \text{else} \end{array} \quad \begin{array}{c} U_{LSQ-09} = 1.25\varepsilon_{LSQ} + U_s \\ U_{LSQ-09} = \min\left(1.25\varepsilon_{LSQ} + U_s, 1.25\Delta_m\right) \\ U_{LSQ-09} = \max\left(1.25\varepsilon_{LSQ} + U_s, 1.25\Delta_m\right) \\ U_{LSQ-09} = 3\Delta_m \end{array} \tag{19}$$

Where $\varepsilon_{LSQ} = f_1 - \bar{f}$ and U_s is the RMS of the fit.

7. SIMULATION RESULTS

Simulations were executed on a commercially available Linux cluster using 320 to 960 cpu cores. Single phase simulations require approximately 500 to 700 iterations and were typically completed in one hour of wall clock time or less. Two-phase boiling simulations require approximately 7000 iterations and could also be completed within two hours by using more cpu cores.

A typical velocity distribution in a plane just above the spacer grid is shown in Figure 7.

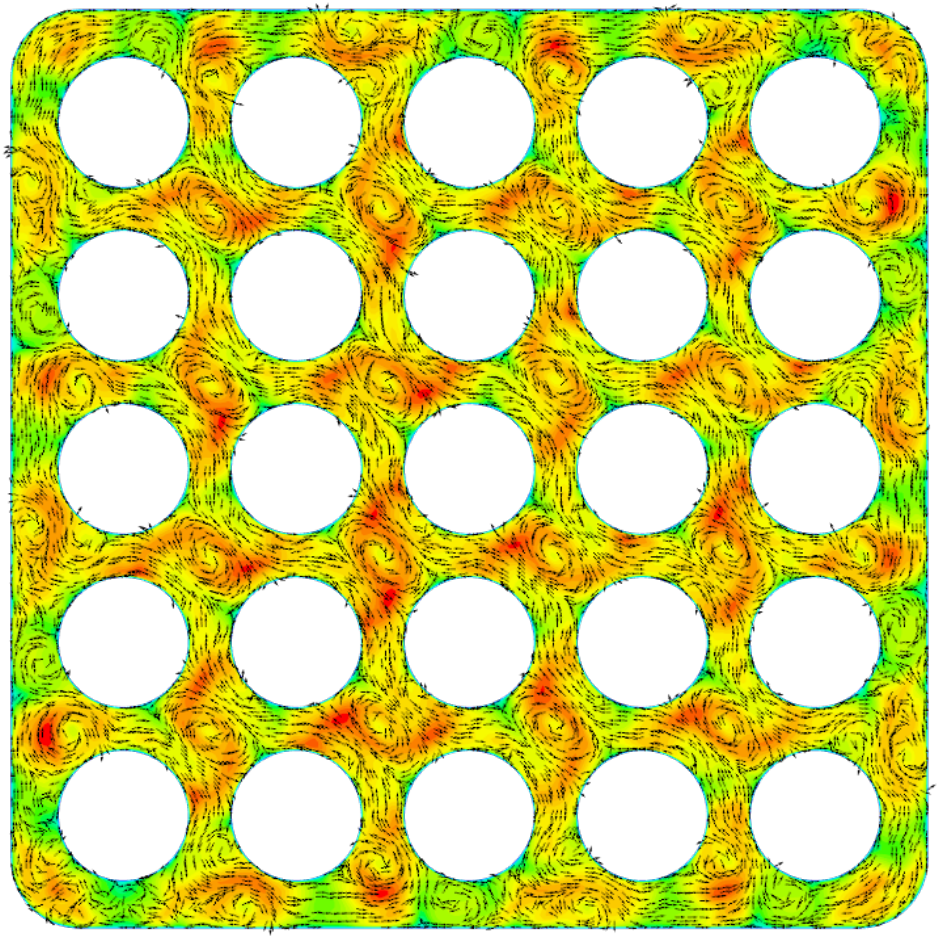

Figure 7. Predicted velocity distribution in a plane just above the final spacer grid.

8. GRID CONVERGENCE RESULTS

To simplify evaluation of grid convergence, data is extracted along a single line probe and a single point probe for all cases and meshes, as shown in Figure 8. The probe is located just above the last spacer grid.

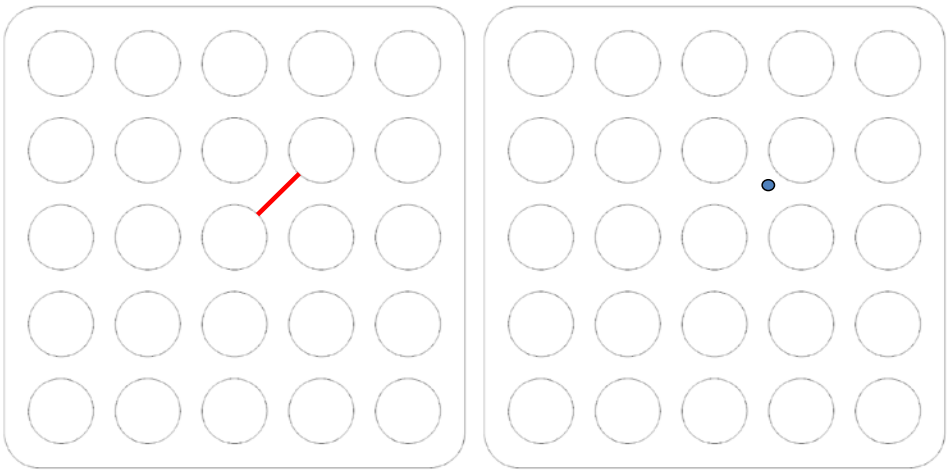

Figure 8. Location of line probe (left) and point probe (right) used for data extraction.

8.1. Case 4 (Isothermal) Results

Grid convergence of selected quantities of interest as predicted by simulations of the isothermal test 4 using the 4 generated meshes has been evaluated both qualitatively and quantitatively. Qualitative comparisons provide insight into the changes in flow structures resulting from mesh refinement. Quantitative assessments using the GCI and LSQ methods provide estimates of uncertainty resulting from the resolution of the finest mesh considered.

8.1.1. Qualitative Assessment

Velocity distributions from each of the four simulations using the generated meshes are shown in Figure 9. In general, all of the meshes are able to resolve the rotational flow features formed by the mixing vanes to some degree. However, the velocity profiles in the models using the two coarser meshes are considerably flattened in comparison to the finer mesh results. This is more apparent in line plots of the total velocity magnitude along the data extraction line, as shown in Figure 10. As a result of the development of more pronounced velocity peaks with refinement the solution is likely oscillatory rather than grid convergence in those regions. The two lateral flow velocity components, also shown in Figure 10, likely show more grid convergent behavior.

Two parameters related to turbulence production and transport, the predicted turbulent kinetic energy and the predicted vorticity magnitude, were also evaluated along the sampling line probe as shown in Figures 11 and 12. Increasing the grid resolution reveals more dynamic profiles of turbulence kinetic energy and vorticity with strong peaks corresponding to the more peaked velocity profile. The fine grid resolution is likely required to adequately resolve these features of the flow field, and these studies should be extended to include additional fine resolution results.

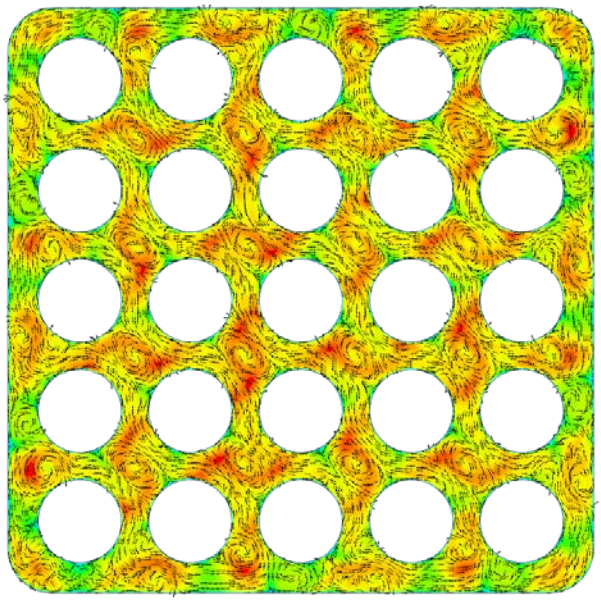

Base = 0.3 mm

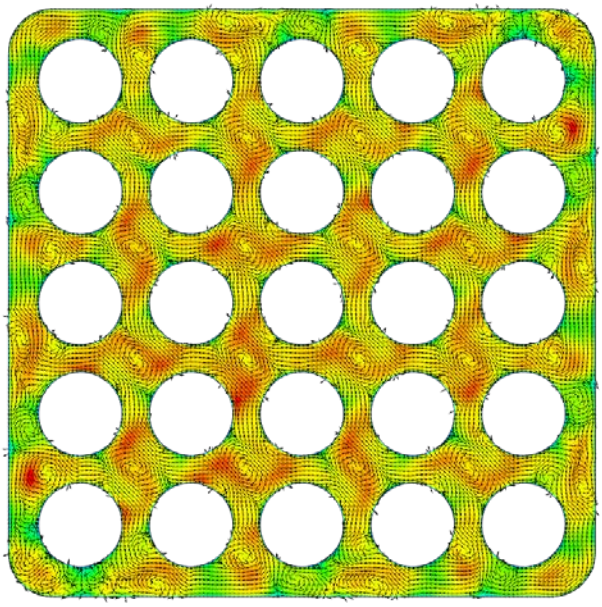

Base = 0.5 mm

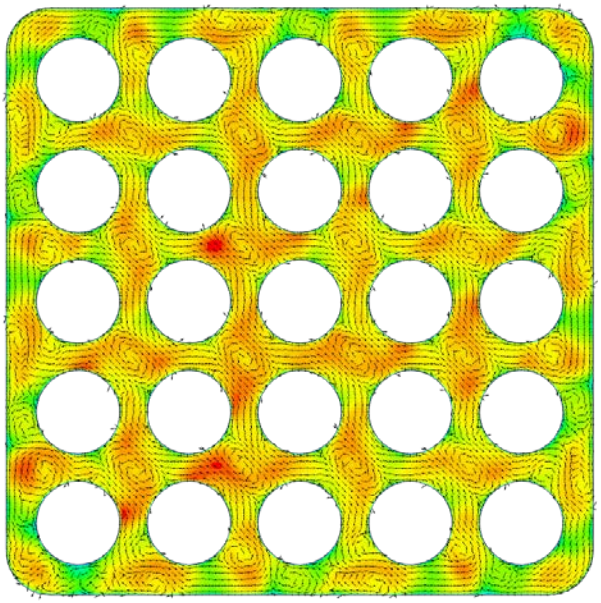

Base = 0.75 mm

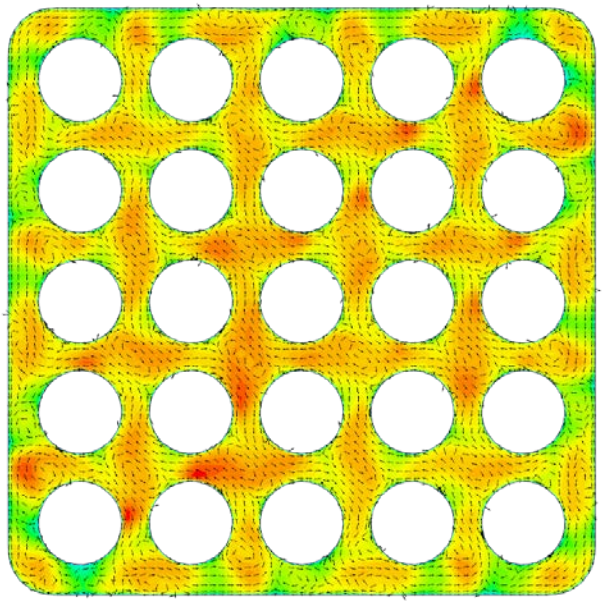

Base = 1.0 mm

Figure 9. Predicted velocity profiles in a lateral plane just above the final spacer grid.

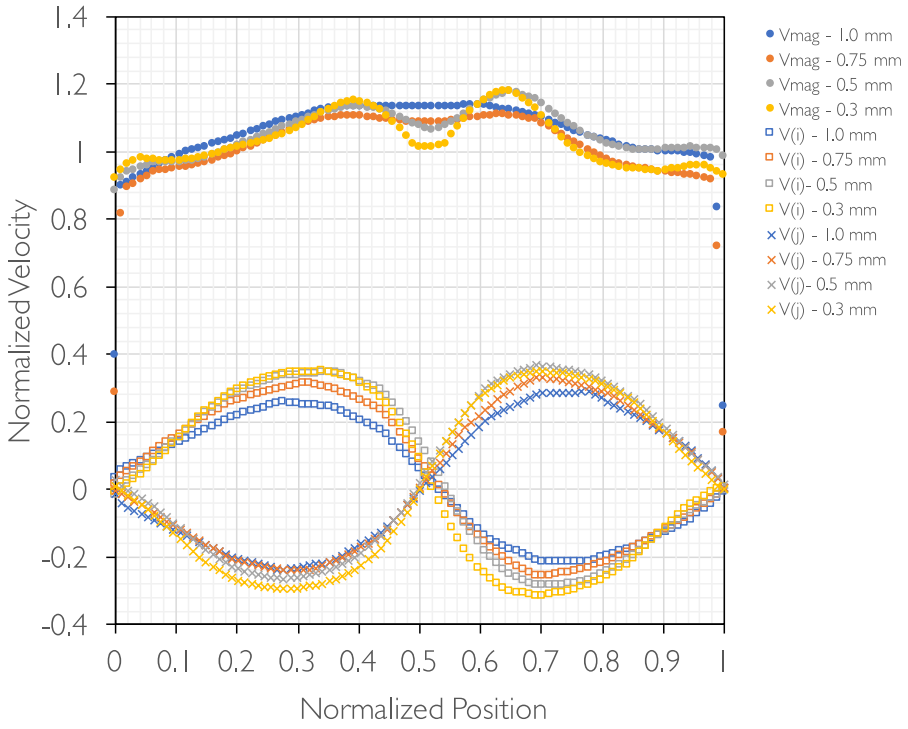

Figure 10. Predicted velocity profiles along the data sampling line for case 4 using all four grids.

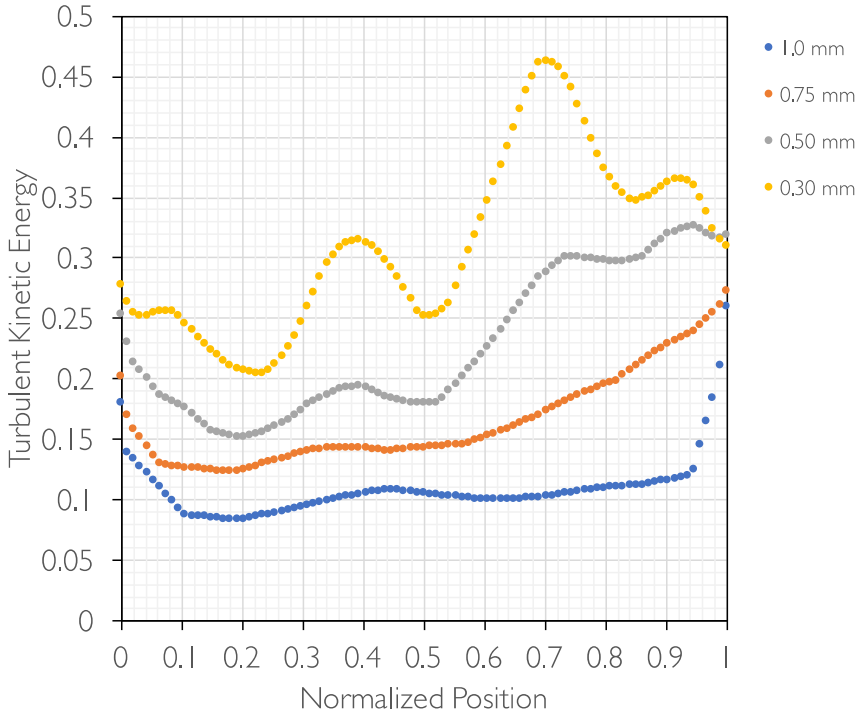

Figure 11. Predicted turbulent kinetic energy profiles along the data sampling line for case 5 using all 4 grids.

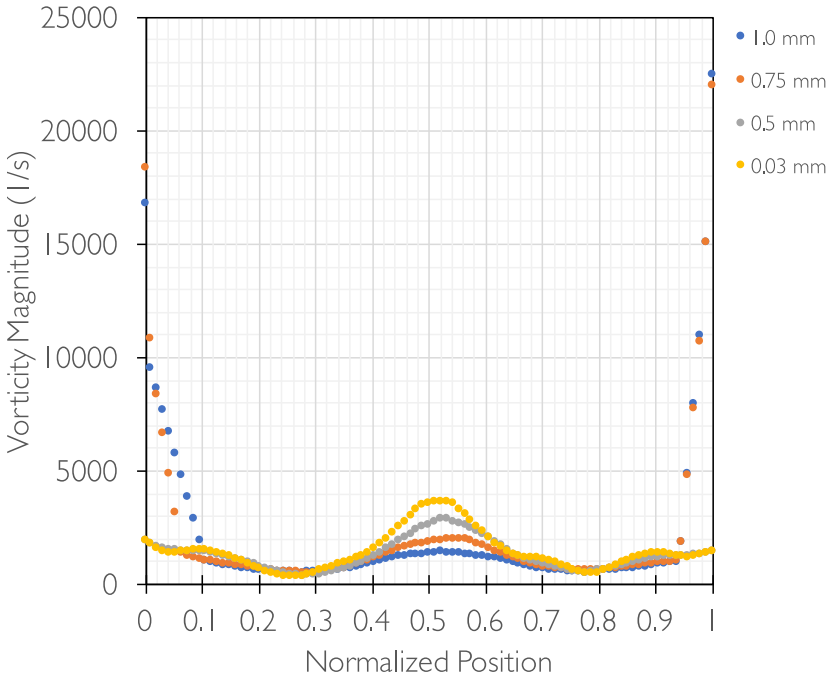

Figure 12. Predicted vorticity (curl of velocity) profiles along the data sampling line for case 4 using all four grids.

8.1.2. Quantitative Assessment

Both the GCI and LSM procedures were applied to selected quantities of interest from the simulations of isothermal case 4. Selected quantities include a mix of global maxima located at any point in the domain, volume averages, surface averages, and data extracted at the monitoring point. For the simulations using each of the four meshes, the characteristic length scale h is shown in Table 3. Calculated refinement ratios, r_{ij}, are shown in Table 4. These values, along with the extracted data itself, where used to evaluate the binary error estimators and the error ratio, R, as shown in Table 5.

Only a few identified parameters produce values of the error ratio, R, between 0 and 1, where grid refinements lead to convergence to some extrapolated value and the GCI method can be applied. Uncertainties were calculated using the grid convergence index and the recommended safety factor of 3.0, as shown in Table 6. While the GCI calculation can be successfully executed for these quantities, the uncertainty estimates produced are not particularly useful because they tend to be very large or very small.

Table 3. Summary of element counts and characteristic mesh dimensions for simulations of case 4 using four generated meshes.

Base (m)	# of Elements	Characteristic Length, h (m)
1.00E-03	17,182,514	7.832E-04
7.50E-04	39,653,550	5.920E-04
5.00E-04	109,797,000	4.212E-04
3.00E-04	421,845,500	2.688E-04

Table 4. Calculated refinement ratios for simulations of case 4 using four generated meshes.

r_{43}	r_{32}	r_{21}
1.32296118	1.405401735	1.566844779

Table 5. Calculated binary errors and error ratio R for simulations of case 4 using four generated meshes.

Quantity	**ε_{43}**	**ε_{32}**	**ε_{21}**	**R**
Maximum Velocity Magnitude, v	-0.382	0.363	-0.060	-0.164
Maximum Velocity Component vi	-0.110	-0.121	-0.106	0.879
Maximum Velocity Component v_j	0.066	-0.725	-0.008	0.010
Maximum Velocity Component v_k	-0.468	0.174	0.186	1.068
Maximum Turb. Kinetic Energy	-0.073	0.565	-3.227	-5.715
Maximum Vorticity ς_i	-3.236E+04	-4.038E+04	-2.333E+05	5.777
Maximum Vorticity ς_j	1.460E+05	-5.421E+04	-1.027E+05	1.894
Maximum Vorticity ς_k	5.106E+03	6.599E+04	-3.849E+05	-5.832
Minimum Wall y+	0.024	-0.046	0.000	0.000
Average Wall y+	-0.270	-0.167	0.242	-1.452
Maximum Wall y+	16.086	26.075	2.429	0.093
Average Outlet Velocity Magnitude	-0.016	-0.011	-0.002	0.210
Velocity Magnitude at Monitor	0.138	-0.179	0.248	-1.385
Velocity Component v_i at Monitor	0.107	0.142	0.077	0.540
Velocity component v_j at Monitor	-0.102	-0.146	0.052	-0.355
Turb. Kinetic Energy at Monitor	-0.080	-0.114	-0.126	1.104
Vorticity ςmag at Monitor	-63.412	37.497	-47.729	-1.273

Table 6. Calculated uncertainties due to grid resolution using the GCI method.

Quantity	f_1	p	e_{GCI}	e_f	U_{GCI}	U_f
Maximum Velocity Component vi	4.971	1.038	0.537	0.179	0.537	0.905
Maximum Velocity Component v_j	5.404	13.445	5.40E-05	1.80E-05	5.40E-05	1.29E-07
Maximum Wall y+	47.075	7.124	0.310	-0.103	0.310	-0.013
Average Outlet Velocity Magnitude	4.005	4.860	9.04E-04	3.01E-04	9.04E-04	1.15E-04
Velocity Component v_i at Monitor	-1.187	7.124	1.507e-7	-0.003	-3.26E-03	-4.16E-04

The LSQ method was applied for the same quantities of interest used in the GCI assessment. Unlike the GCI method, the LSQ method can provide an error estimate for any convergence condition because it allows for a default uncertainty estimate of three times the maximum difference between sampled values, even when the least squares analysis fails to produce an estimate of the order of accuracy. Results of the assessment of the uncertainty, U_{LSQ-09}, are shown in Table 7. Those quantities of interest focused on global maxima are still poorly suited for grid convergence uncertainty estimation, even with the LSQ approach, possibly because the global maxima are not necessarily tied to a single point in the domain space. This is significant since the current DNB identification algorithm relies on identification of such maxima; this further underscores the importance of the ongoing development effort to enable DNB identification based on local surface data rather than relying on identification of global maxima. Resulting uncertainties for local or average quantities are generally less than 20% of the predicted value from the finest mesh solution.

Table 7. Calculated uncertainties due to grid resolution using the LSQ method.

Quantity	f_1	p	Δm	1.25 ε_{LSQ} + Us	U_{LSQ-09}
Maximum Velocity Magnitude, v	7.378	N/A	0.382	N/A	1.147
Maximum Velocity Component vi	4.971	0.730	0.338	1.250	0.355
Maximum Velocity Component v_j	5.404	0.545	0.732	1.414	0.916
Maximum Velocity Component v_k	6.925	N/A	0.468	N/A	1.405
Maximum Turb. Kinetic Energy	6.872	0.000	3.227	3.227	4.034
Maximum Vorticity $ç_i$	5.54E+05	N/A	3.06E+05	N/A	9.18E+05
Maximum Vorticity $ç_j$	3.06E+05	N/A	1.57E+05	N/A	4.71E+05
Maximum Vorticity $ç_k$	5.27E+05	N/A	3.85E+05	N/A	1.15E+06
Minimum Wall y+	0.283	0.000	0.046	0.046	0.057
Average Wall y+	18.686	0.000	0.437	0.437	0.546
Maximum Wall y+	47.075	1.769	44.589	46.801	21.407
Average Outlet Velocity Magnitude	4.005	2.732	0.030	3.445	0.038
Velocity Magnitude at Monitor	4.040	4.745	0.248	6.179	0.309
Velocity Component v_i at Monitor	-1.187	1.060	0.325	1.650	0.228
Velocity component v_j at Monitor	1.351	3.119	0.249	4.147	0.311
Turb. Kinetic Energy at Monitor	0.426	0.094	0.319	0.436	0.399
Vorticity çmag at Monitor	624.010	N/A	73.644	N/A	220.932

8.2. Case 9 (Two-Phase Boiling) Results

The same four computational meshes used in the single-phase isothermal simulations of case 4 were also used in simulations of the two-phase boiling flow in case 9. DNB simulations using the Generation 1A modeling approach are executed as a series of pseudo-steady-state evaluations. The power level is increased incrementally and allowed to reach a steady state before the next increment. Case 9, which has a reduced power level and, consequently, produces only small amounts of steam on the pin surfaces, is consistent with one of the intermediate steps before DNB is reached. With vapor volume fractions below 1×10^{-5}, vapor production can be expected to have only a small influence on the flow field.

As in the evaluation of mesh sensitivity for the isothermal case 4, the effects of mesh resolution are evaluated both qualitatively and quantitatively for case 9.

8.2.1. Qualitative Assessment

The velocity field predicted by the simulation using the finest grid in the lateral cross-section just above the uppermost spacer grid is shown in Figure 13. The rotational flow structures observed in

the isothermal case 4 simulations remain and predicted flow fields are qualitatively quite similar in spite of the small differences in flow rate, small differences in thermophysical properties resulting from inlet temperature and the activation of the two-phase models. As in the prior case, the peak velocity magnitudes associated with the rotational elements are only captured in the most refined meshes, as indicated in Figure 14. Comparisons of turbulent kinetic energy in Figure 15 and vorticity in Figure 16. The predicted temperature fields from each of the four cases at the same elevation are compared in Figure 17 and exhibit a strong oscillatory grid convergence behavior.

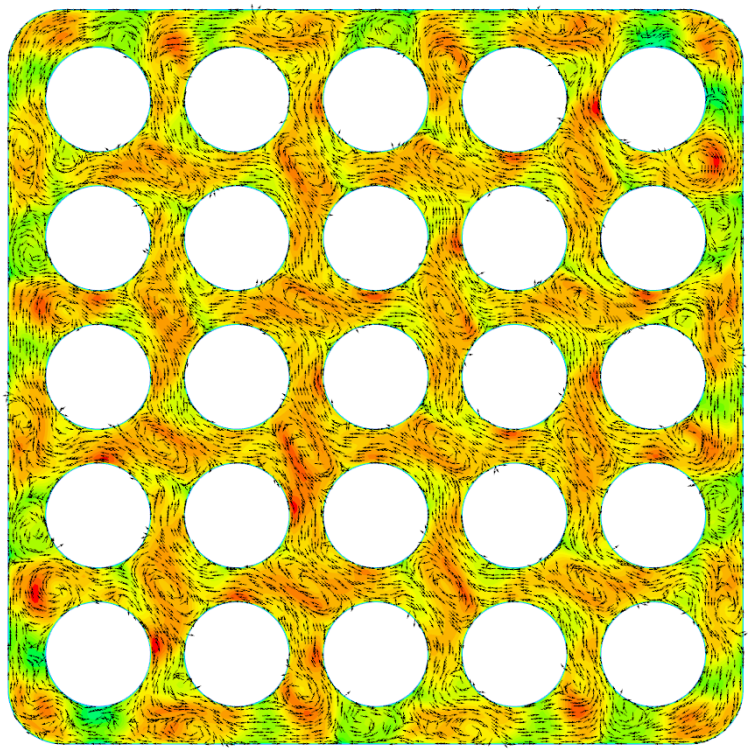

Figure 13. Predicted velocity profile in the lateral cross section just above the last spacer grid for case 9 using the finest resolution grid.

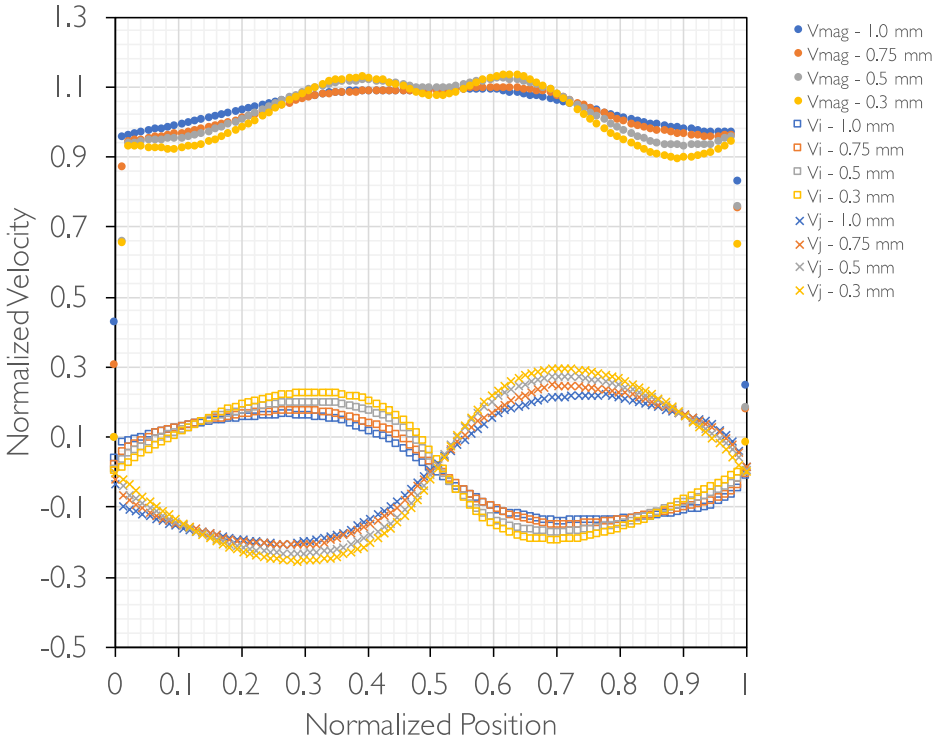

Figure 14. Predicted velocity profiles along the data sampling line for case 9 using all four grids.

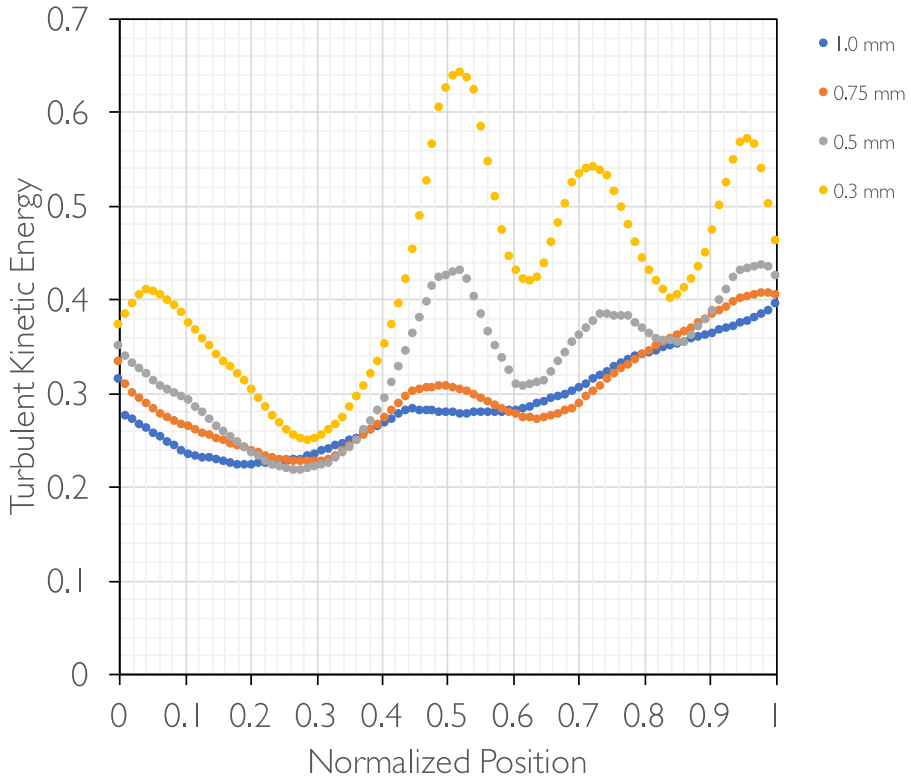

Figure 15. Predicted turbulent kinetic energy profiles along the data sampling line for case 9 using all four grids.

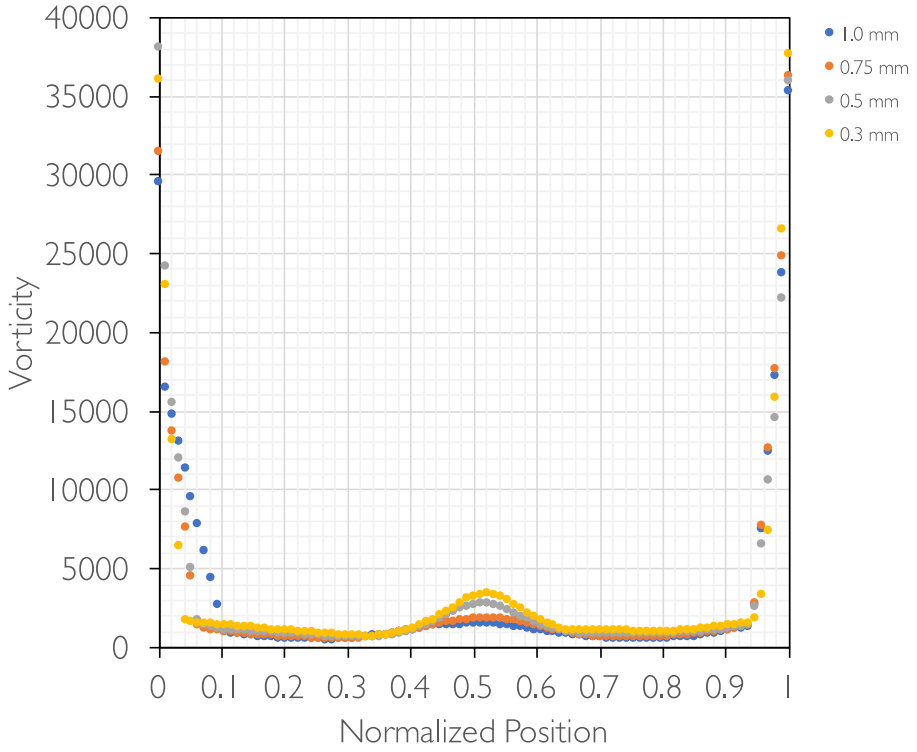

Figure 16. Predicted vorticity profiles along the data sampling line for case 9 using all four grids.

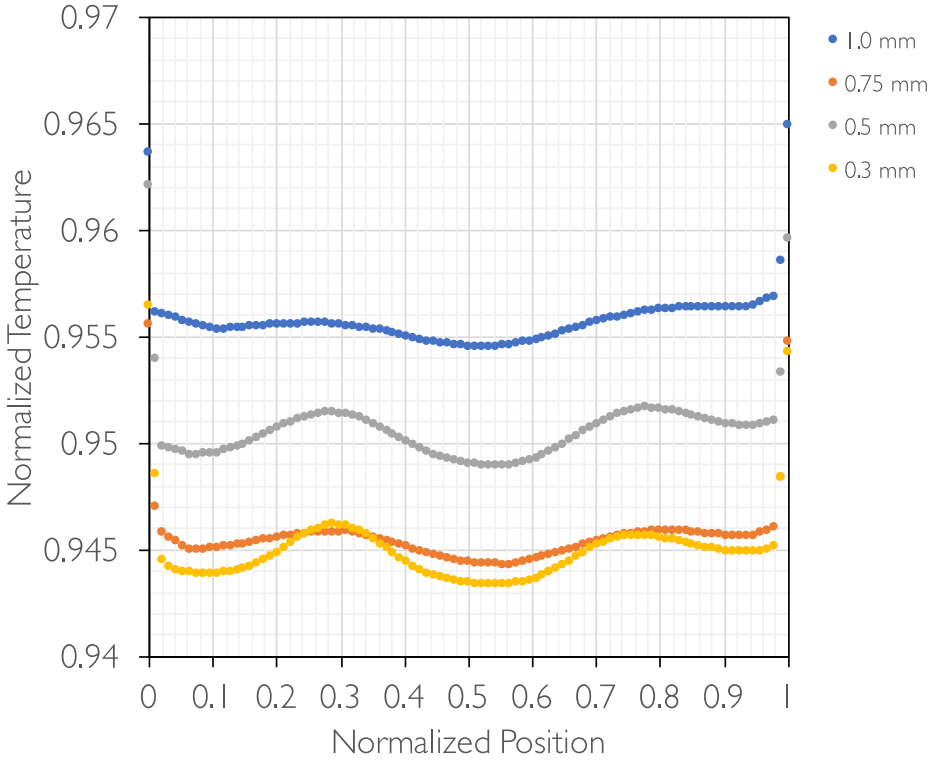

Figure 17. Predicted temperature profiles along the data sampling line for case 9 using all four grids.

8.2.2. Quantitative Assessment

As in the previous case, both the GCI and LSQ methods for evaluation of uncertainty resulting from computational mesh resolution were applied to selected quantities of interest. Since the previous case demonstrated that the methods cannot be applied to evaluations of global maxima within the solution the subset of quantities to be considered was focused on surface average and monitoring point data. The geometric parameters shown in Table 3 and 4 remain valid for these cases since the same meshes are used. Calculated binary errors and the error ration R are shown in Table 8 for the selected parameters. The evaluation of the error ratio suggests that the GCI method can only be applied to the monitoring point values of the j-direction velocity vector component and monitoring point vorticity magnitude. The GCI uncertainties are shown in Table 9 for these parameters. Large uncertainties are again observed for the evaluation of local vorticity.

As in the previous case, the LSQ method was also applied. Evaluated uncertainties shown in Table 10 are similar in magnitude to those observed for the isothermal case 4.

Table 8. Calculated binary errors and error ratio R for simulations of case 9 using four generated meshes.

Quantity	e43	e32	e21	R
Outlet Liquid Velocity	0.004	-0.002	-0.022	9.823
Outlet Vapor Velocity	0.005	-0.006	-0.010	1.742
Liq. Velocity Magnitude v at Monitoring Point	-0.008	0.074	0.118	1.596
Liq. Velocity Component v_i at Monitoring Point	0.046	0.107	0.123	1.147
Liq. Velocity Component v_j at Monitoring Point	-0.129	-0.161	-0.129	0.804
Liq. Turb. Kinetic Energy at Monitoring Point	0.008	-0.063	-0.132	2.079
Liq. Vorticity Magnitude ς at Monitoring Point	-1.225E+02	-1.809E+02	-1.737E+02	0.960
Liq. Temperature at Monitoring Point	1.034E-02	-5.788E-03	5.905E-03	-1.020

Table 9. Calculated uncertainties in simulations of case 9 due to grid resolution as evaluated using the GCI method.

Quantity	f1	p	eGCI	ef	UGCI	Uf
Liq. Velocity Component v_i at Monitoring Point	1.788	1.270	0.505	0.168	0.505	0.658
Liq. Vorticity Magnitude ς at Monitoring Point	995.9	0.812	1185.4	395.1	1185.4	2696.1

Table 10. Calculated uncertainties in simulations of case 9 due to grid resolution as evaluated using the LSQ method.

Quantity	f1	p	Δm	$1.25\ e_{LSQ} + U_s$	U_{LSQ-09}
Outlet Liquid Velocity	6.258	-1e-5	0.024	2396.3	0.0729
Outlet Vapor Velocity	6.318	0.1283	0.016	2361.5	0.021
Liq. Velocity Magnitude v at Monitoring Point	6.289	0.1273	0.191	3.99E+03	2.39E-01
Liq. Velocity Component v_i at Monitoring Point	-1.159	N/A	0.275	N/A	0.826
Liq. Velocity Component v_j at Monitoring Point	1.788	0.266	0.419	1208.2	0.524
Liq. Turb. Kinetic Energy at Monitoring Point	0.514	N/A	0.195	N/A	0.585
Liq. Vorticity Magnitude ς at Monitoring Point	995.9	N/A	477.1	N/A	1431.4
Liq. Temperature at Monitoring Point	586.5	N/A	6.483	N/A	19.45

9. CONCLUSION

A baseline meshing strategy has been established for simulations of DNB in the Westinghouse 5 x 5 rod bundle facility. Qualitative assessments of the sensitivity of simulation predictions of local and global flow field characteristics suggest that mesh resolution should be similar to the finer to grids used in this study to adequately resolve the effects of the mixer vane spacer grid. Quantitative assessments using the GCI and LSQ methods suggest that grid convergence or even uncertainty due to grid resolution cannot be established for predictions of global maxima using either method. This is significant because the Generation 1A DNB detection algorithm is reliant on identification of global maximum pin surface temperature as the primary indication that DNB has occurred. This outcome reinforces the importance of the ongoing effort to establish an alternative method based on local rather than global criteria, for which the grid uncertainty can generally be established by the LSQ method.

10. REFERENCES

[1] E. Baglietto and M. A. Christon, *Demonstration and Assessment of Advanced Modeling Capabilities for Multiphase Flow with Sub-cooled Boiling*, CASL Technical Report. CASL-U-2013-0181-001 (2013).
[2] Description of Mixing Vane Grid CHF test for CASL DNB Challenge Problem. Tech. rep. PFT-16-3, Rev.1. 2016.
[3] STAR-CCM+ User Guide, v. 12.02 (2017).
[4] R. Brewster, et al., Application of CD-adapco Best Practices to NESTOR OMEGA MVG Benchmark Exercises using STAR-CCM+," Proc. Of NURETH-16, Chicago, IL, August 30-September 4, 2015
[5] L. Eca and M. Hoekstra, "An Evaluation of Verification Procedures for CFD Applications," Presented at the 24th Symposium on Naval Hydrodynamics, July 2002.
[6] Phillips, T., "Extrapolation-based discretization error and uncertainty estimation in computational fluid dynamics." Thesis, Virginia Polytechnic University (2012).